

Unveiling the impact of residual Li conversion and cation ordering on electrochemical performance of Co-free Ni-rich cathodes

Chu Wang¹, Lei Tan², Hongling Yi¹, Zixiang Zhao¹, Xiaoli Yi³, Youyuan Zhou⁴, Junchao Zheng³, Jiexi Wang³, Lingjun Li^{1,*}

Nano Res., **Just Accepted Manuscript** • <https://doi.org/10.1007/s12774-022-4889-0>

<http://www.thenanoresearch.com> on Aug. 10, 2022

© Tsinghua University Press 2022

Just Accepted

This is a “Just Accepted” manuscript, which has been examined by the peer-review process and has been accepted for publication. A “Just Accepted” manuscript is published online shortly after its acceptance, which is prior to technical editing and formatting and author proofing. Tsinghua University Press (TUP) provides “Just Accepted” as an optional and free service which allows authors to make their results available to the research community as soon as possible after acceptance. After a manuscript has been technically edited and formatted, it will be removed from the “Just Accepted” Web site and published as an ASAP article. Please note that technical editing may introduce minor changes to the manuscript text and/or graphics which may affect the content, and all legal disclaimers that apply to the journal pertain. In no event shall TUP be held responsible for errors or consequences arising from the use of any information contained in these “Just Accepted” manuscripts. To cite this manuscript please use its Digital Object Identifier (DOI®), which is identical for all formats of publication.

Unveiling the impact of residual Li conversion and cation ordering on electrochemical performance of Co-free Ni-rich cathodes

Chu Wang¹, Lei Tan², Hongling Yi¹, Zixiang Zhao¹, Xiaoli Yi³, Youyuan Zhou⁴,
Junchao Zheng³, Jiexi Wang³, Lingjun Li^{1,*}

¹ *School of Materials Science and Engineering, Changsha University of Science and
Technology, Changsha, Hunan 410114, PR China*

² *School of Energy and Power Engineering, Changsha University of Science and
Technology, Changsha, Hunan 410114, PR China*

³ *School of Metallurgy and Environment, Central South University, Changsha, Hunan
410083, PR China*

⁴ *Hunan Changyuan Lico Co. Ltd., Changsha, Hunan 410205, PR China*

* Corresponding author.

E-mail address: lingjun.li@csust.edu.cn (L. Li)

Abstract:

The residual Li and $\text{Li}^+/\text{Ni}^{2+}$ cation mixing play essential roles in the electrochemical properties of Ni-rich cathodes. However, a general relationship between the residual Li conversion, cation mixing, and their effects on the Li^+ kinetics and structural stability has yet to be established, due to the presence of cobalt in the cathode. Here, we explore the synergistic impact of the residual Li conversion and cation ordering on a Co-free Ni-rich cathode (i.e., $\text{LiNi}_{0.95}\text{Mn}_{0.05}\text{O}_2$). It discloses that the rate capability is mainly affected by residual Li contents and operating voltage. Specifically, residual Li can be electrochemically converted to cathode electrolyte interphase (CEI) below 4.3 V, thus inducing high interphase resistance, and decomposes to produce CO_2 -dominated gas at 4.5 V, causing temporary enhancement of Li^+ diffusivity but severe surface degradation during cycling. Moreover, the cycling performance of Co-free Ni-rich cathode is not only determined by $\text{Li}^+/\text{Ni}^{2+}$ cation-ordered superlattice, which enhances the structural stability as it functions as the pillar to impede lattice collapse at a highly charged state, but also by the robust CEI layers which protect the bulk from electrolyte attack under 4.3 V. These findings promote an in-depth understanding of residual Li conversion and $\text{Li}^+/\text{Ni}^{2+}$ cation ordering on Co-free Ni-rich cathode.

Keywords: Li-ion batteries; Co-free Ni-rich cathodes; residual Li conversion; cation ordering

1 Introduction

The rapid expansion of electric vehicles (EVs) in recent years is closely related to the application of advanced lithium-ion batteries (LIBs). The properties of the cathodes have great influence on the electrochemical performance of LIBs[1-3].

Layered Ni-rich oxide cathodes, such as $\text{LiNi}_{1-x-y}\text{Co}_x\text{Al}_y\text{O}_2$ and $\text{LiNi}_{1-x-y}\text{Co}_x\text{Mn}_y\text{O}_2$ (NCA, NCM, $x+y \leq 0.2$), have been extensively explored, owing to the high energy density and good rate capability [4, 5]. Nevertheless, high Ni contents would increase the probability of Ni^{2+} migrating to the Li^+ slab, and vice versa, to form cation mixing, which substantially influences on the performance of cathodes [6, 7]. Several studies have been proceeded to investigate the effect of cation mixing on Ni-rich cathodes. It is reported that the cation mixing will increase the activation energy barrier and hindrance for Li^+ migration, thus deteriorating the rate capability and cycling performance [8, 9]. However, it is also discovered that the Ni^{2+} ions, which orderly occupy Li^+ sites (cation-ordered structure), can hinder the pernicious phase transitions and collapse of the layered structure at a deeply charged state [10]. Up to now, the functionality of cation mixing in Ni-rich cathodes remains controversial.

This controversy may ascribe to the presence of Co element in ternary NCM and NCA systems. According to previous studies, Co^{3+} can obscure the effects of cation mixing on Ni-rich cathodes in the following ways: (1) Co^{3+} serves as a buffer atom to relieve magnetic frustration and thereby stabilize the layered structure of cathodes, which is identical to the function of $\text{Li}^+/\text{Ni}^{2+}$ cation ordering [11]. (2) Co^{3+} can enhance the electrical conductivity because of the overlap between $\text{Co}^{3+/4+}$ redox pair

and O 2p orbital, whereas cation mixing may hamper the mobility of Li⁺ by decreasing the thickness of lattice interlayer [12]. (3) Co³⁺ can provide extra capacity when oxidized to Co⁴⁺ at a highly charged state, which would mitigate the capacity decay induced by inactive Ni²⁺ in the Li⁺ slab [13]. Thus, to achieve a comprehensive understanding of cation mixing on Ni-rich cathodes and resolve the contradictory statements reported by previous works, Co-free Ni-rich LiNi_{1-x}Mn_xO₂ (x < 0.1) cathode materials are suitable choices for the research object.

During the high-temperature synthesis of Co-free Ni-rich cathodes, residual Li will form due to the excessive addition of lithium sources [14, 15]. The residual Li would react with electrolyte to generate gases, resulting in poor cycle stability and battery safety [16, 17]. In contrast, previous work reports residual Li can protect cathode materials from close contact with the electrolyte, thus avoiding surface degradation and improving cycling performance [18]. The reason for these disparate understandings of residual Li conversion on Ni-rich cathode is mainly attributed to the amount of residual Li and operating voltage range, which will be discussed detailly in this study.

Hence, revealing the effects of residual Li conversion and cation mixing is essential for developing advanced Co-free Ni-rich cathodes. In this work, LiNi_{0.95}Mn_{0.05}O₂ with relatively high (denoted as NM95-H) and low (denoted as NM95-L) contents of residual Li and cation mixing are synthesized by adjusting the calcination temperature. By conducting structural analysis and electrochemical testing, we disclose that both residual Li and operating voltage account for the discrepancy of

rate performance. For the first time, we discover that the cyclability of the Co-free Ni-rich cathode can be attributed to not only $\text{Li}^+/\text{Ni}^{2+}$ cation-ordered structure impeding lattice collapse at a highly charged state, but also residual Li, protecting cathode from electrolyte attack by converting to robust cathode electrolyte interphase (CEI).

2 Experimental

2.1 Materials synthesis

The Co-free Ni-rich $\text{LiNi}_{0.95}\text{Mn}_{0.05}\text{O}_2$ cathodes were prepared through a solid-state calcination method. Specifically, the $\text{Ni}_{0.95}\text{Mn}_{0.05}(\text{OH})_2$ precursors (Hunan Changyuan Lico Co. Ltd.) were blended with $\text{LiOH}\cdot\text{H}_2\text{O}$ (excess of 5 mol.%) using a mortar and placed into a tube furnace after the grind. Subsequently, the obtained mixed powders were calcinated at 480 °C for 5 h for a preheat, then sintered at 700 °C or 750 °C for another 10 h to obtain the final products. The whole calcination process is under an O_2 atmosphere, with 5 °C min^{-1} for the heating rate.

2.2 Materials characterization

The morphological characteristics of prepared cathodes were collected using scanning electron microscopy (SEM, LSM 7900F, JEOL). The chemical compositions of Ni and Mn elements in each cathode were determined by inductively coupled plasma atomic emission spectrometry (ICP-AES, Agilent 7900 ICP-MS). The particle size distributions were collected by a particle size analyzer (Mastersizer 3000). The crystallographic structures of as-prepared samples were analyzed by X-ray diffraction

(D8 Advance, Bruker) using Cu K α radiation. The detection angle is 10°-90° and 10°-120°, and the scan speed is 5° min⁻¹. The Rietveld refinement were conducted with the Rietica software. The residual Li contents are detected by the titration method. Specifically, 2 g of cathode materials are put into purified water (100 mL) and then stirred for 10 minutes. The obtained solution was filtered and then titrated with 0.048 mol/L HCl. The phenolphthalein and methyl red served as pH indicators. Surface analysis of cathodes is performed by the X-ray photoelectron spectroscopy (XPS) method (VG MultiLab 2000). The microstructure of cathodes is investigated by transmission electron microscopy (TEM, Titan G2 60-300) and scanning transmission electron microscopy (STEM, FEI Titan Themis). For TEM analysis of activated or cycled cathodes, the cell was disassembled in a glove box under an inert atmosphere, followed by DMC washing to remove electrolyte. The cross-sectional sample of cycled cathodes at charged state is prepared using the focused ion beam (FIB) method (FEI Helios NanoLab 600i). For gas generation analysis, operando differential electrochemical mass spectrometry (DEMS) were conducted by mass spectrometer (HPR-40, Hiden Analytical). The cells for DEMS analysis were charged to 4.3 V or 4.5 V (versus Li/Li⁺) at 0.1 C.

2.3 Electrochemical tests

CR2025 coin-type cells with Li metal anodes were assembled to assess the electrochemical performance. The active materials, acetylene black and polyvinylidene difluoride (with a weight ratio of 8:1:1) are blended in a mortar and then dissolved in *N*-methyl-2-pyrrolidone to form a slurry. Subsequently, the slurry is

coated on aluminum foil, accompanied by a drying procedure in a vacuum oven for almost 4 h (120 °C). After punching, the dried foil was transformed into thin disks with a diameter of 12 mm and electrode loading of 2.2 mg cm⁻². The electrolyte comprises the LiPF₆ solute and solvent containing dimethyl carbonate, ethyl methyl carbonate, and ethylene carbonate (DMC, EMC, EC, 1:1:1 in volumetric ratio). The assembly of coin-type half-cells was performed in a glove box, filled with inert Ar gas. After rest for at least 8 h, the cells were transferred into a thermostatic tank (30 °C) for the electrochemical test, using the BTS-testing system (Neware, China). **The cells were firstly activated for 3 cycles at 0.1 C between 2.7-4.3 V or 2.7-4.5 V (1 C = 180 mA g⁻¹), and then tested at a cut-off voltage of 4.3 V (abbreviated as NM95-H@4.3V, NM95-H@4.5V, NM95-L@4.3V and NM95-L@4.5V, respectively).** Electrochemical workstation (CHI 660E) is used to probe the electrochemical impedance spectroscopy (EIS), with the frequency range varying from 10⁻³ to 10⁵ Hz. The galvanostatic intermittent titration technique (GITT) was tested to calculate the diffusion coefficients of Li⁺ (D_{Li⁺}) for all cathodes, and details for the testing process have been described in our previous work [19, 20].

3 Results and discussion

3.1 Morphology and structure

The SEM images about the Ni_{0.95}Mn_{0.05}(OH)₂ precursor and NM95 cathodes are shown in Fig. S1(a)-S1(c). Both hydroxide precursor and cathodes exhibit a spherical morphology, but their primary particles are micro sheet-like and cubic shapes, respectively. **The chemical compositions of each cathode determined by ICP-AES are**

in good accordance with the intended values (Table S1). The NM95-H and NM95-L cathodes exhibit similar and nearly monodisperse particle size distribution, with an average diameter of 11.1 μm (Fig. S2). The XRD patterns as displayed in Fig. S3 reveal that all cathode materials exhibit a layered $\alpha\text{-NaFeO}_2$ structure (R-3m space group), and the peaks designated to impurities are undetectable. The peak intensity ratio of (003)/(104) is 1.78 for NM95-H and 1.88 for NM95-L respectively, indicating that NM95-H cathodes possess a higher cation mixing degree than that of NM95-L [21]. The refinements of XRD patterns (Fig. 1(a) and 1(b), Table S2 and S3) show exactly quantitative results of cation mixing, with 4.45% for NM95-H and 2.82% for NM95-L, respectively. This result is also confirmed by XPS data of Ni 2p (Fig. S4), showing more Ni^{2+} contents on the NM95-H surface than that of the NM95-L.

It is widely accepted that for Ni-rich layered cathode, the residual Li compound increase with cation mixing, because the calcination process is a lithiation process [22, 23]. The titration method is utilized to quantify the residual Li, and the details of the titration processes are described in the experimental section [24, 25]. As shown in Fig. 1(c), the weight ratio of residual Li (LiOH and Li_2CO_3) for NM95-H is 2.70 wt.%, which is higher than 1.55 wt.% of NM95-L cathode. This result is further confirmed by the XPS method (Fig. 1(d)-1(f)). The characteristic peaks of Li_2CO_3 or $\text{LiOH/Li}_2\text{CO}_3$ in C 1s, Li 1s, and O 1s are located at 289.9, 55.4, and 531.6 eV, respectively. Specifically, the proportion of Li_2CO_3 or $\text{LiOH/Li}_2\text{CO}_3$ in C 1s, Li 1s, and O 1s for NM95-H cathode is 34.0%, 74.6%, 84.2%, which is higher than that of the NM95-L. The microstructures of NM95-H and NM95-L are characterized by

TEM. Both two cathodes develop a layered structure, and the thickness of amorphous residual Li on the NM95-H cathode surface is approximately 2.2 nm (Fig. 1(g)), while the NM95-L cathode shows no obvious amorphous layer on the surface (Fig. 1(h)).

3.2 Rate capability analysis

The electrochemical properties of NM95-H@4.3V and NM95-L@4.3V are evaluated between 2.7-4.3 V at 30 °C. Compared with NM95-H@4.3V, NM95-L@4.3V cathode owns a higher initial discharging capacity and Coulombic efficiency of 216.2 mAh g⁻¹ and 86.70%, respectively (Fig. 2(a)). Besides, NM95-L@4.3V exhibits superior rate capability than NM95-H@4.3V (Fig. 2(b)), especially at high-rate current. The discharge capacity of NM95-L@4.3V and NM95-H@4.3V is 121.1 and 98.9 mAh g⁻¹ at 10 C. Consequently, too much cation mixing and residual Li would limit the rate performance.

To verify the detailed different impacts of cation mixing and residual Li on the rate performance, cathodes are electrochemically activated at 2.7-4.5 V for 3 cycles, then tested between 2.7-4.3 V at 30 °C. Compared with NM95-H@4.3V, the rate performance of NM95-H@4.5V is improved, delivering a higher capacity (115.62 mAh g⁻¹) at 10 C (Fig. 2(c)), which benefits from the possible removal of residual Li. On the contrary, the capacity of NM95-L@4.5V declines sharply, with only 98.32 mAh g⁻¹ at 10 C (Fig. 2(d)), suggesting the undesirable side reaction as charging to high voltage. Galvanostatic intermittent titration technique (GITT) is performed to compare diffusion coefficients of Li⁺ (D_{Li^+}), during the discharging process from 4.3-2.7 V after a different-voltage activation process. As shown in Fig. 2(e),

NM95-H@4.5V exhibits a relatively higher D_{Li^+} than NM95-H@4.3V. EIS further shows that the surface film impedance (R_f) of NM95-H@4.5V (18.2 Ω) is lower than that of NM95-H@4.3V (21.8 Ω , Fig. S5(a), Table S4) [26, 27]. As reported early, residual Li leads to sluggish D_{Li^+} and high interphase resistance [28]. Therefore, we highly speculate that residual Li would be removed after activation at 4.5V, and the rate capability of the NM95 cathode is closely related to the residual Li contents and working voltage.

3.3 Variations of CEI

To further understand the underlying mechanism of residual Li decomposition and CEI production after the activation process for NM95 cathodes, XPS spectra and TEM images of NM95 cathodes activated under different voltage ranges are shown in Fig. 3 and Fig. 4, respectively. XPS analysis confirms that residual Li will be electrochemically converted into CEI after activation. As shown in Fig. 3, the surfaces of all NM95 cathodes show typical CEI characteristics, mainly comprising lithium alkyl carbonates (Li_2CO_3 , $ROCO_2Li$), LiF, Li_xPF_y , and $Li_xPO_yF_z$ species [29-31]. The high intensity of LiF peak in F 1s of NM95-H@4.3V cathode is attributed to the high concentration of Li_2CO_3 on the pristine material, and LiF is beneficial to form a robust CEI [32, 33].

The TEM images confirm that NM95-H@4.3V cathode possesses a thick and uniform CEI of approximately 3.06 nm (Fig. 4(a) and Fig. S6(a)), consistent with the lowest peak intensity in Ni 2p spectra but the highest one of CEI compositions in Li 1s spectra (Fig. S7). In marked contrast to the NM95-H@4.3V, the NM95-H@4.5V

shows a thin and uneven CEI of approximately 0.78 nm (Fig. 4(b) and Fig. S6(b)). Operando differential electrochemical mass spectrometry (DEMS) shows more CO₂ released from NM95-H//Li cell when charged to 4.5V (Fig. 4(e) and 4(f)), demonstrating the decomposition of Li₂CO₃ as this formula: $\text{Li}_2\text{CO}_3 - 2\text{e}^- \rightarrow 2\text{Li}^+ + 1/2 \text{O}_2 + \text{CO}_2$ [19]. The thin CEI could decrease the interphase resistance and benefit Li⁺ kinetics, which conforms to above-mentioned rate performance.

Besides, the NM95-L@4.3V exhibits a thin and uneven CEI of approximately 0.65 nm (Fig. 4(c) and Fig. S6(c)), consistent with the scarcely amorphous layer of NM95-L in Fig. 1(h). However, after activation at 4.5 V for 3 cycles, the NiO peak in O 1s spectra (Fig. 3(f)) and FFT images of the cycled electrode demonstrate the irreversible phase transition from layer structure to rock-salt phase at the surface of NM95-L@4.5V (Fig. 4(d) and Fig. S6(d)). The XRD patterns of electrochemically activated cathodes in Fig. S8 show that the (003) diffraction peak of NM95-L@4.5V cathode shifts to a lower angle compared with other cathodes, which is further verifying the reconstruction of the Li-deficient phase of NM95-L@4.5V. The surface reconstruction with layer-rock salt phase transition could block the Li⁺ diffusion and consequently undermine the rate capability of NM95-L@4.5V in Fig. 2(d).

Based on the obtained results, Fig. 5 vividly illustrates the intrinsic correlation among the residual Li contents, voltage range, and CEI characteristics. The thick residual Li on the NM95-H surface can be converted into a thick and uniform CEI layer below 4.3 V, incurring high interphase resistance. Compared with the NM95-H@4.3V, the thick CEI decomposes to gas at a cut-off voltage of 4.5 V, and

the rate performance of NM95-H is substantially improved. In addition, the small amount of residual Li on the NM95-L cathode surface turns into a thin and uneven CEI layer below 4.3 V, and leaves the bare surface of NM95-L in direct contact with electrolyte at 4.5 V, resulting in a severe surface degradation as well as sluggish Li⁺ kinetics. Therefore, the rate performance of Co-free Ni-rich cathodes is mainly attributed to the residual Li contents and operating voltage. **The thick CEI on NM95-H@4.3V cathode would increase the interfacial impedance and thus reduce the ionic conductivity, while the thin CEI on NM95-H@4.5V and NM95-L@4.3V cathodes promote Li⁺ diffusion.**

3.4 Cycling stability

The cycling performance of NM95-H@4.3V and NM95-L@4.3V cathodes are shown in Fig. 6(a). After 100 cycles between 2.7-4.3 V at 1 C, NM95-H@4.3V and NM95-L@4.3V cathodes retain 98.16% and 80.41% of their initial capacities, respectively. Fig. 6(b) and 6(c) compared the cycling performance of NM95-H and NM95-L cathodes activated at different voltages for solely investigating the impact of residual Li on structure stability. For NM95-H cathodes, the CEI layer on NM95-H@4.3V (as shown in Fig. 4(a)) protects the cathode surface from electrolyte attack, thereby maintaining the original layered structure during cycles, whereas the increased cut-off voltage could induce residual Li decomposes, and the bare surface of NM95-H@4.5V directly contacts with electrolyte, causing detrimental surficial phase transitions with the capacity retention of 84.33%. For NM95-L cathodes, the inactive NiO layers (as shown in Fig. 4(d)) form on NM95-L@4.5V cathode surface as

charging to high voltage, which would be mainly responsible for the faster capacity loss (capacity retention of 63.49%) during cycles.

Furthermore, Fig. 6(d) and 6(e) show TEM and corresponding FFT images of NM95-H@4.3V and NM95-L@4.3V cathodes after 100 cycles between 2.7-4.3 V. The FFT patterns of the marked region (Fig. 6(d-I), 6(e-I) and 6(e-II)) confirm that the cycled NM95-H@4.3V cathode still maintains its original structure due to the protection of CEI layer, which derives from thick residual Li by electrochemical conversion, while the surface of cycled NM95-L@4.3V cathode degrades from layered structure to rock-salt phase because of the side reaction with electrolyte. Besides, the (003) peak of NM95-L@4.3V shifts to a lower angle, indicating more serious structural degradations than NM95-H@4.3V (Fig S9). However, this protection effect disappears between 2.7-4.5 V due to the decomposition of residual Li, and thus cause battery swelling at such high voltage (Fig. 4(b) and 4(f)). Therefore, the residual Li can convert into robust CEI and stabilize the cathode surficial structure during cycles between 2.7-4.3 V, but arouses potential safety problems between 2.7-4.5 V.

It is noteworthy that the capacity retention of NM95-H@4.5V (84.33%) is higher than NM95-L@4.3V (80.41%), although the NM95-H@4.5V suffers battery swelling problem, and both samples show the same surface properties after electrochemical activation for 3 cycles at 0.1 C (Fig. 4(b) and 4(c)). This difference may be due to the bulk structural evolution of the material caused by cation mixing, as the cation mixing ratio of NM95-H (4.45%) is higher than NM95-L (2.82%). The dQ/dV^{-1} curves of

NM95-H@4.5V and NM95-L@4.3V cathodes show H1→M→H2→H3 multiple phase transitions (Fig. 7(a)-7(c)), in which H and M represent hexagonal and monoclinic structure respectively [26, 34]. The abrupt contraction of the c-axis in unit cell during the H2→H3 phase transition stage would induce stress concentrations between grains, which can cause cracks in cathode particles during cycles. Subsequently, the electrolyte will penetrate via those cracks to react with cathodes, thereby deteriorating the reversibility of capacity [35, 36]. Apparently, the intensity of H2→H3 oxidation peak for NM95-L@4.3V of the first cycle is significantly higher and it drops more quickly after 100 cycles than that of NM95-H@4.5V, indicating a drastic phase transition with poor reversibility, which is detrimental to structural integrity.

To further understand the effect of cation mixing on the structural stability of NM95 cathodes, the bulk structures of the charged NM95-H@4.5V and NM95-L@4.3V after 100 cycles between 2.7-4.3 V are demonstrated by cross-sectional images and STEM images (Fig. 7(d) and 7(e)), prepared by the focused ion beam (FIB) method. The NM95-H@4.5V cathode shows no distinct cracks, while some of the long and wide cracks cross the NM95-L@4.3V particle. The superior structure stability of NM95-H@4.5V originates from the partially ordered structure with Li⁺ occupied Ni²⁺ site orderly and vice versa, as the absence of Co³⁺ is conducive to forming an ordering of cations in Ni-rich cathode materials [37]. This cation-ordered superlattice causes extra diffraction spots (marked by yellow circles) in SAED patterns (Fig. 7(d-I)), which keep a simple fraction relationship with

basic diffraction spots, indicating the origin of them from a $\text{Li}^+/\text{Ni}^{2+}$ ordered structure rather than a secondary phase [10, 38]. The presence of Li^+ in Ni^{2+} slabs, as a pillar, is assumed to impede lattice collapse induced by phase transitions at a highly charged state [39]. However, the layered structure of NM95-L@4.3V cathode suffers from severe phase transitions and consequently cracks. Those cracks can serve as channels to facilitate electrolyte penetration into the interior of particles, reacting with cathode to form NiO phase (Fig. 7(e-II)), which would be responsible for cycling stability degradation of NM95-L cathode. Fig. 7(f) and 7(g) illustrate the crystal structure of both cation-ordered superlattices and layered structures viewed from the different axis, which corresponds to Fig. 7(d-I) and 7(e-I), respectively.

4 Conclusion

In summary, we synthesized Co-free Ni-rich $\text{LiNi}_{0.95}\text{Mn}_{0.05}\text{O}_2$ cathodes with different residual Li contents and cation mixing degrees. Without the disturbance of the Co element, the actual impacts of residual Li conversion and cation-ordered superlattice on Ni-rich cathodes have been discovered. The residual Li can be electrochemically converted into the CEI layer during electrochemical activation, which is mainly responsible for the decrease of rate performance due to its high resistance to Li^+ diffusivity. While as the cut-off voltage raises to 4.5 V, the residual Li decomposes to CO_2 -dominated gas, resulting in enhanced Li^+ kinetics temporarily but more severe surface degradation during cycling. In addition, according to the STEM analysis, the $\text{Li}^+/\text{Ni}^{2+}$ cation-ordered superlattices can inhibit phase transition at a highly charged state and suppress microcrack generation during cycles owing to the

pillar effect. However, the cation-ordering is not the only reason for the enhanced cycling performance of NM95-H between 2.7-4.3 V. By utilizing various measurements, we reveal that the converted CEI layer can prevent the cathode from electrolyte attack and inhibit side reaction under 4.3 V, thus synergistically improving the cycling stability of Co-free Ni-rich oxide cathodes. This research proposes a systematic understanding of residual Li conversion and cation ordering on Co-free Ni-rich cathode, which provides a specific guide for cathode design to promote the application of LIBs.

Acknowledgement

This work was financially supported by the National Natural Science Foundation of China (No. 51774051), the Science and Technology Planning Project of Hunan Province (No. 2019RS2034), the Hunan High-tech Industry Science and Technology Innovation Leading Plan (2020GK2072), the Changsha City Fund for Distinguished and Innovative Young Scholars (No. KQ1707014).

References

- [1] Luo, D.;Fan, J.;Yao, Z.;Xie, H.;Cui, J.;Yang, Y.;Ding, X.;Ji, J.;Wu, S.;Ling, M. et al. An almost full reversible lithium-rich cathode: Revealing the mechanism of high initial coulombic efficiency. *J. Energy Chem.* **2021**, *62*, 120-126.
- [2] Zou, Y. G.;Mao, H.;Meng, X. H.;Du, Y. H.;Sheng, H.;Yu, X.;Shi, J. L.;Guo, Y. G. Mitigating the kinetic hindrance of single-crystalline Ni-rich cathode via surface gradient penetration of tantalum. *Angew. Chem. Int. Ed.* **2021**, *60*, 26535-26539.
- [3] Liu, Y.;Chen, Y.;Wang, J.;Wang, W.;Ding, Z.;Li, L.;Zhang, Y.;Deng, Y.;Wu, J.;Chen, Y. Hierarchical yolk-shell structured Li-rich cathode boosting cycling and

voltage stabled LIBs. *Nano Res.* **2021**, *15*, 3178-3186.

- [4] Nam, G. W.; Park, N. Y.; Park, K. J.; Yang, J.; Liu, J.; Yoon, C. S.; Sun, Y. K. Capacity fading of Ni-rich NCA cathodes: effect of microcracking extent. *ACS Energy Lett.* **2019**, *4*, 2995-3001.
- [5] You, B.; Wang, Z.; Shen, F.; Chang, Y.; Peng, W.; Li, X.; Guo, H.; Hu, Q.; Deng, C.; Yang, S. et al. Research progress of single - crystal nickel - rich cathode materials for lithium ion batteries. *Small Methods* **2021**, *5*, 2100234.
- [6] Du, Y. H.; Sheng, H.; Meng, X. H.; Zhang, X. D.; Zou, Y. G.; Liang, J. Y.; Fan, M.; Wang, F.; Tang, J.; Cao, F. F. et al. Chemically converting residual lithium to a composite coating layer to enhance the rate capability and stability of single-crystalline Ni-rich cathodes. *Nano Energy* **2022**, *94*, 106901.
- [7] Wu, F.; Liu, N.; Chen, L.; Li, N.; Dong, J.; Lu, Y.; Tan, G.; Xu, M.; Cao, D.; Liu, Y. et al. The nature of irreversible phase transformation propagation in nickel-rich layered cathode for lithium-ion batteries. *J. Energy Chem.* **2021**, *62*, 351-358.
- [8] Zou, Y. H.; Yang, X. F.; Lv, C. X.; Liu, T. C.; Xia, Y. Z.; Shang, L.; Waterhouse, G. I. N.; Yang, D. J.; Zhang, T. R. Multishelled Ni-rich $\text{Li}(\text{Ni}_x\text{Co}_y\text{Mn}_z)\text{O}_2$ hollow fibers with low cation mixing as high-performance cathode materials for Li-ion batteries. *Adv. Sci.* **2017**, *4*, 1600262.
- [9] Liu, W.; Oh, P.; Liu, X.; Lee, M. J.; Cho, W.; Chae, S.; Kim, Y.; Cho, J. Nickel-rich layered lithium transition-metal oxide for high-energy lithium-ion batteries. *Angew. Chem. Int. Ed.* **2015**, *54*, 4440-4457.
- [10] Kim, U. H.; Park, G. T.; Son, B. K.; Nam, G. W.; Liu, J.; Kuo, L.; Kaghazchi, P.; Yoon, C. S.; Sun, Y. K. Heuristic solution for achieving long-term cycle stability for Ni-rich layered cathodes at full depth of discharge. *Nat. Energy* **2020**, *5*, 860-869.
- [11] Li, M.; Lu, J. Cobalt in lithium-ion batteries. *Science* **2020**, *367*, 979-980.
- [12] Choi, J. U.; Voronina, N.; Sun, Y. K.; Myung, S. T. Recent progress and perspective of advanced high - energy Co - less Ni - rich cathodes for Li - ion batteries: yesterday, today, and tomorrow. *Adv. Energy Mater.* **2020**, *10*, 2002027.

- [13] Liu, T.; Yu, L.; Liu, J.; Lu, J.; Bi, X.; Dai, A.; Li, M.; Li, M.; Hu, Z.; Ma, L. et al. Understanding Co roles towards developing Co-free Ni-rich cathodes for rechargeable batteries. *Nat. Energy* **2021**, *6*, 277-286.
- [14] Cho, D. H.; Jo, C. H.; Cho, W.; Kim, Y. J.; Yashiro, H.; Sun, Y. K.; Myung, S. T. Effect of residual lithium compounds on layer Ni-rich $\text{Li}[\text{Ni}_{0.7}\text{Mn}_{0.3}]\text{O}_2$. *J. Electrochem. Soc.* **2014**, *161*, A920-A926.
- [15] Zhang, S. S. Problems and their origins of Ni-rich layered oxide cathode materials. *Energy Storage Mater.* **2020**, *24*, 247-254.
- [16] Seong, W. M.; Cho, K. H.; Park, J. W.; Park, H.; Eum, D.; Lee, M. H.; Kim, I. S.; Lim, J.; Kang, K. Controlling residual lithium in high-nickel (>90 %) lithium layered oxides for cathodes in lithium-ion batteries. *Angew. Chem. Int. Ed.* **2020**, *59*, 18662-18669.
- [17] Xu, G. L.; Liu, X.; Daali, A.; Amine, R.; Chen, Z.; Amine, K. Challenges and strategies to advance high - energy nickel - rich layered lithium transition metal oxide cathodes for harsh operation. *Adv. Funct. Mater.* **2020**, *30*, 2004748.
- [18] Zhang, J. T.; Tan, X. H.; Guo, L. M.; Jiang, Y.; Liu, S. N.; Wang, H. F.; Kang, X. H.; Chu, W. G. Controllable formation of lithium carbonate surface phase during synthesis of nickel-rich $\text{LiNi}_{0.9}\text{Mn}_{0.1}\text{O}_2$ in air and its protection role in electrochemical reaction. *J. Alloys Compd.* **2019**, *771*, 42-50.
- [19] Li, L.; Chen, J.; Huang, H.; Tan, L.; Song, L.; Wu, H. H.; Wang, C.; Zhao, Z.; Yi, H.; Duan, J. et al. Role of residual Li and oxygen vacancies in Ni-rich cathode materials. *ACS Appl. Mater. Interfaces* **2021**, *13*, 42554-42563.
- [20] Li, L.; Fu, L.; Li, M.; Wang, C.; Zhao, Z.; Xie, S.; Lin, H.; Wu, X.; Liu, H.; Zhang, L. et al. B-doped and $\text{La}_4\text{NiLiO}_8$ -coated Ni-rich cathode with enhanced structural and interfacial stability for lithium-ion batteries. *J. Energy Chem.* **2022**. <https://doi.org/10.1016/j.jechem.2022.04.037>.
- [21] Ryu, H. H.; Park, N. Y.; Yoon, D. R.; Kim, U. H.; Yoon, C. S.; Sun, Y. K. New class of Ni - rich cathode materials $\text{Li}[\text{Ni}_x\text{Co}_y\text{B}_{1-x-y}]\text{O}_2$ for next lithium batteries. *Adv. Energy Mater.* **2020**, *10*, 2000495.

- [22] Wang, D.;Kou, R.;Ren, Y.;Sun, C. J.;Zhao, H.;Zhang, M. J.;Li, Y.;Huq, A.;Ko, J. Y. P.;Pan, F. et al. Synthetic control of kinetic reaction pathway and cationic ordering in high-ni layered oxide cathodes. *Adv. Mater.* **2017**, *29*, 1606715.
- [23] Wang, S.;Hua, W.;Missyul, A.;Darma, M. S. D.;Tayal, A.;Indris, S.;Ehrenberg, H.;Liu, L.; Knapp, M. Kinetic control of long - range cationic ordering in the synthesis of layered Ni - rich oxides. *Adv. Funct. Mater.* **2021**, *31*, 2009949.
- [24] Seong, W. M.;Kim, Y.; Manthiram, A. Impact of residual lithium on the adoption of high-nickel layered oxide cathodes for lithium-ion batteries. *Chem. Mater.* **2020**, *32*, 9479-9489.
- [25] Kim, Y.;Park, H.;Warner, J. H.; Manthiram, A. Unraveling the intricacies of residual lithium in high-Ni cathodes for lithium-ion batteries. *ACS Energy Lett.* **2021**, *6*, 941-948.
- [26] Yang, H. P.;Wu, H. H.;Ge, M.;Li, L. J.;Yuan, Y. F.;Yao, Q.;Chen, J.;Xia, L. F.;Zheng, J. M.;Chen, Z. Y. et al. Simultaneously dual modification of Ni - rich layered oxide cathode for high - energy lithium - ion batteries. *Adv. Funct. Mater.* **2019**, *29*, 1808825.
- [27] Ke, C. Z.;Liu, F.;Zheng, Z. M.;Zhang, H. H.;Cai, M. T.;Li, M.;Yan, Q. Z.;Chen, H. X.; Zhang, Q. B. Boosting lithium storage performance of Si nanoparticles via thin carbon and nitrogen/phosphorus co-doped two-dimensional carbon sheet dual encapsulation. *Rare Met.* **2021**, *40*, 1347-1356.
- [28] Liu, Y.;Tang, L. B.;Wei, H. X.;Zhang, X. H.;He, Z. J.;Li, Y. J.; Zheng, J. C. Enhancement on structural stability of Ni-rich cathode materials by in-situ fabricating dual-modified layer for lithium-ion batteries. *Nano Energy* **2019**, *65*, 104043.
- [29] Fan, X.;Ou, X.;Zhao, W.;Liu, Y.;Zhang, B.;Zhang, J.;Zou, L.;Seidl, L.;Li, Y.;Hu, G. et al. In situ inorganic conductive network formation in high-voltage single-crystal Ni-rich cathodes. *Nat. Commun.* **2021**, *12*, 5320.
- [30] Feng, X.;Wu, H. H.;Gao, B.;Świętosławski, M.;He, X.; Zhang, Q. Lithiophilic N-doped carbon bowls induced Li deposition in layered graphene film for

- advanced lithium metal batteries. *Nano Res.* **2021**, *15*, 352-360.
- [31] Cai, M.;Zhang, H.;Zhang, Y.;Xiao, B.;Wang, L.;Li, M.;Wu, Y.;Sa, B.;Liao, H.;Zhang, L. et al. Boosting the potassium-ion storage performance enabled by engineering of hierarchical MoSSe nanosheets modified with carbon on porous carbon sphere. *Sci. Bull.* **2022**, *67*, 933-945.
- [32] Sheng, H.;Meng, X. H.;Xiao, D. D.;Fan, M.;Chen, W. P.;Wan, J.;Tang, J.;Zou, Y. G.;Wang, F.;Wen, R. et al. An air-stable high-nickel cathode with reinforced electrochemical performance enabled by convertible amorphous Li_2CO_3 modification. *Adv. Mater.* **2022**, *34*, e2108947.
- [33] Liu, W.;Li, J.;Li, W.;Xu, H.;Zhang, C.; Qiu, X. Inhibition of transition metals dissolution in cobalt-free cathode with ultrathin robust interphase in concentrated electrolyte. *Nat. Commun.* **2020**, *11*, 3629.
- [34] Heenan, T. M. M.;Wade, A.;Tan, C.;Parker, J. E.;Matras, D.;Leach, A. S.;Robinson, J. B.;Llewellyn, A.;Dimitrijevic, A.;Jervis, R. et al. Identifying the origins of microstructural defects such as cracking within Ni - rich NMC811 cathode particles for lithium - ion batteries. *Adv. Energy Mater.* **2020**, *10*, 2002655.
- [35] Sun, H. H.; Manthiram, A. Impact of microcrack generation and surface degradation on a nickel-rich layered $\text{Li}[\text{Ni}_{0.9}\text{Co}_{0.05}\text{Mn}_{0.05}]\text{O}_2$ cathode for lithium-ion batteries. *Chem. Mater.* **2017**, *29*, 8486-8493.
- [36] Li, H.;Liu, A.;Zhang, N.;Wang, Y.;Yin, S.;Wu, H.; Dahn, J. R. An unavoidable challenge for Ni-rich positive electrode materials for lithium-ion batteries. *Chem. Mater.* **2019**, *31*, 7574-7583.
- [37] Aishova, A.;Park, G. T.;Yoon, C. S.; Sun, Y. K. Cobalt - free high - capacity Ni - rich layered $\text{Li}[\text{Ni}_{0.9}\text{Mn}_{0.1}]\text{O}_2$ cathode. *Adv. Energy Mater.* **2019**, *10*, e1903179.
- [38] Kim, U. H.;Park, G. T.;Conlin, P.;Ashburn, N.;Cho, K.;Yu, Y. S.;Shapiro, D. A.;Maglia, F.;Kim, S. J.;Lamp, P. et al. Cation ordered Ni-rich layered cathode for ultra-long battery life. *Energy Environ. Sci.* **2021**, *14*, 1573-1583.

- [39] Yoon, C. S.; Choi, M. J.; Jun, D. W.; Zhang, Q.; Kaghazchi, P.; Kim, K. H.; Sun, Y. K. Cation ordering of Zr-doped LiNiO₂ cathode for lithium-ion batteries. *Chem. Mater.* **2018**, *30*, 1808-1814.

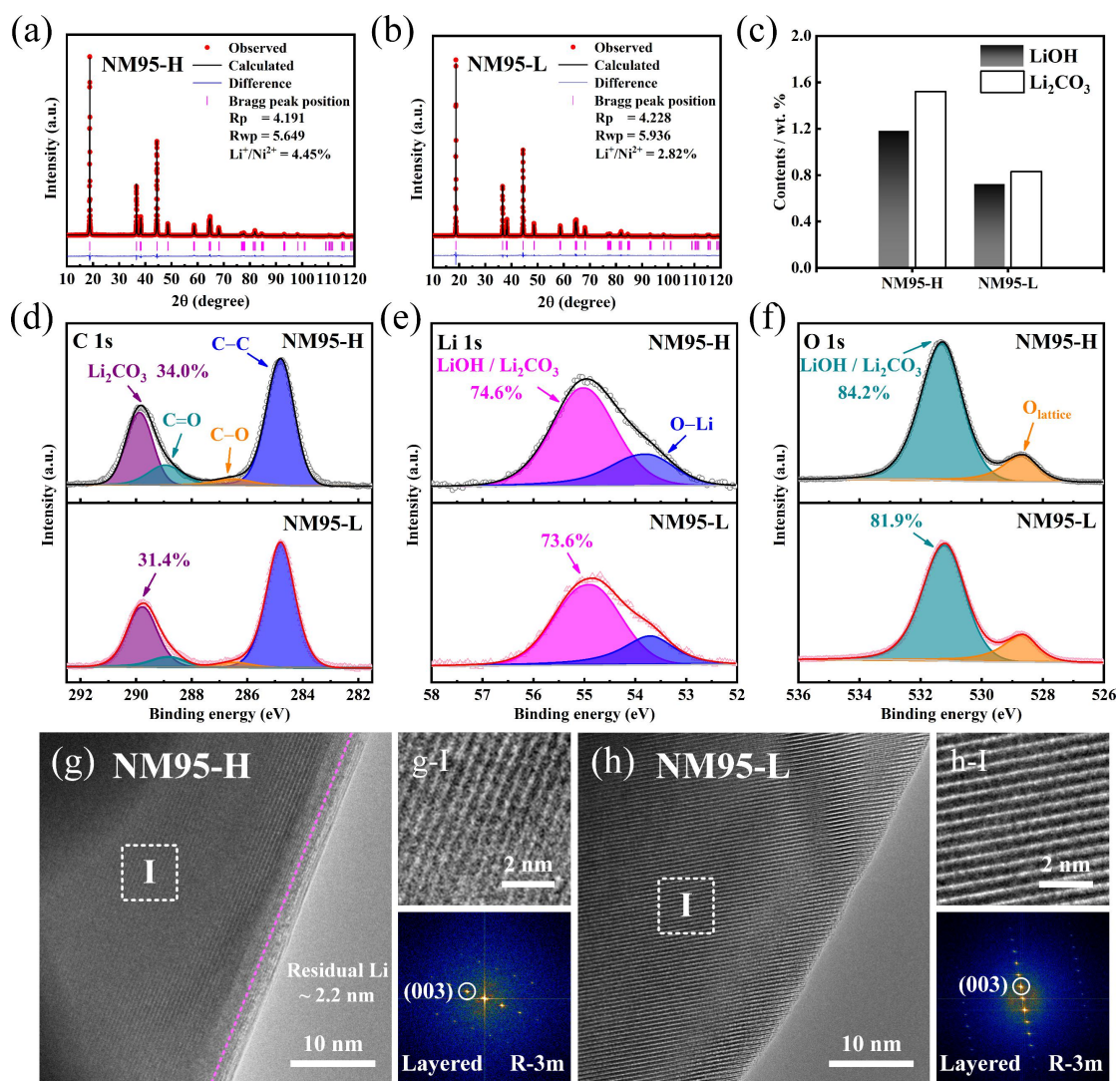


Fig. 1. XRD refinement results of (a) NM95-H and (b) NM95-L. (c) Residual Li determined by the titration method. (d-f) XPS spectra of C 1s, Li 1s and O 1s. TEM images of (g) NM95-H and (h) NM95-L cathodes, accompanied by (g-I, h-I) magnifications of marked areas and FFT images.

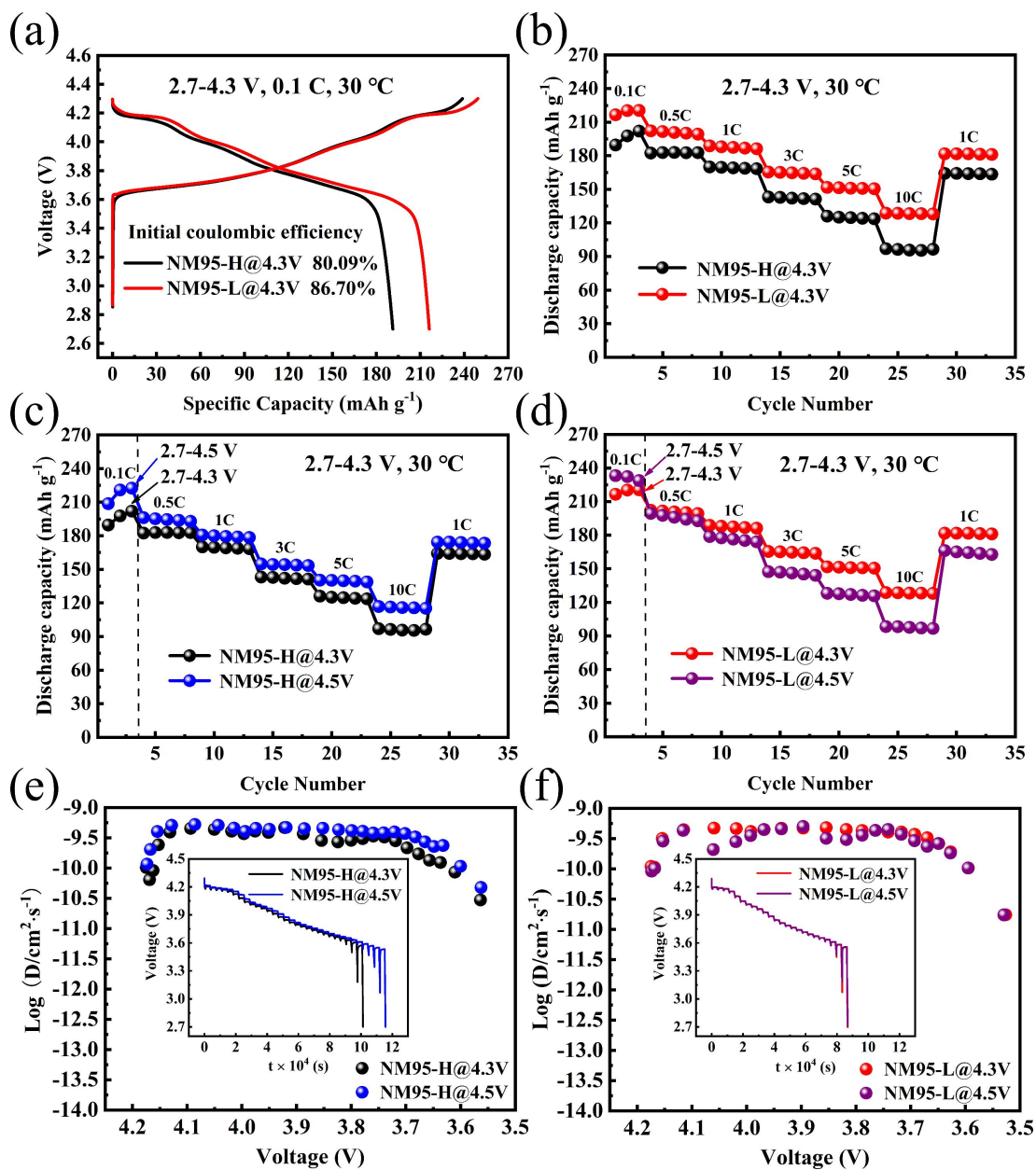


Fig. 2. (a) Initial charge and discharge curves of NM95-H@4.3V and NM95-L@4.3V cathodes. (b-d) Rate capability of NM95-H and NM95-L cathodes after electrochemical activation at different voltage ranges. GITT curves of electrochemically activated (e) NM95-H and (f) NM95-L cathodes during discharging process from 4.3-2.7 V.

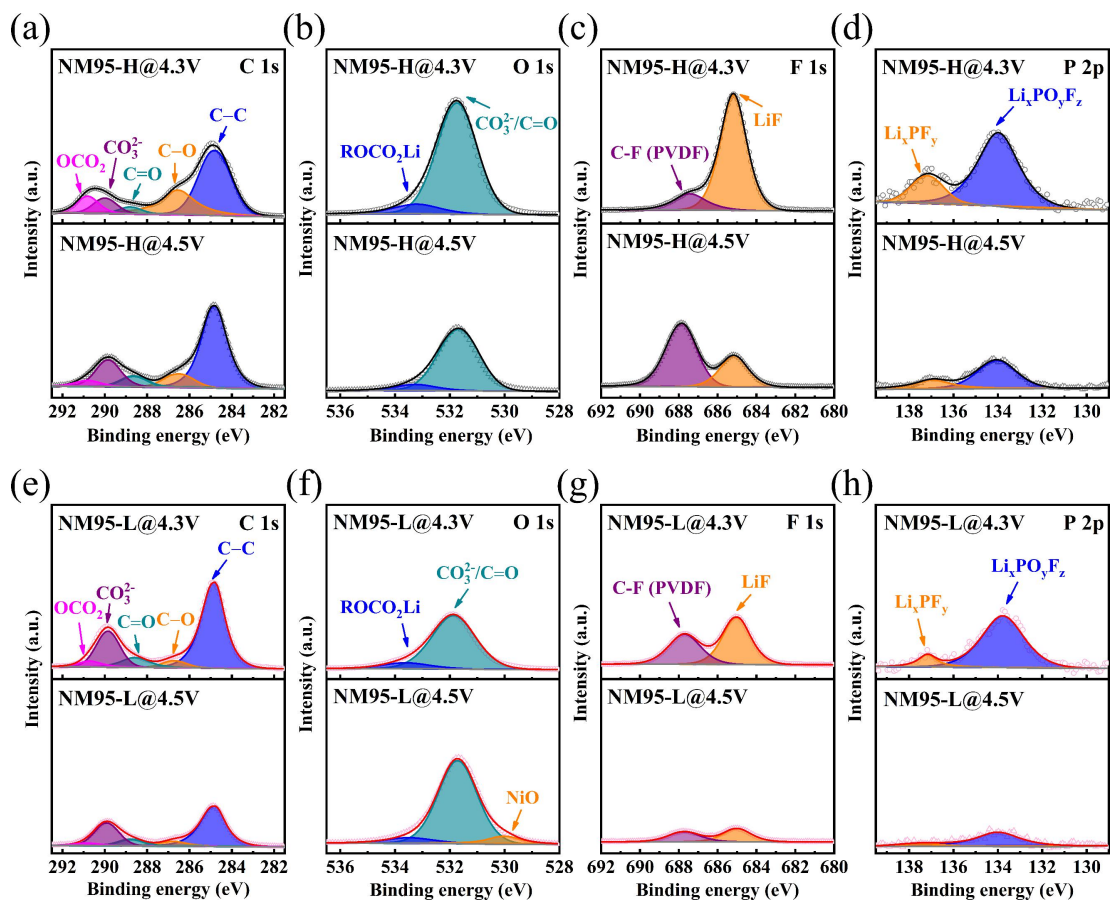


Fig. 3. (a-h) XPS spectra of C 1s, O 1s, F 1s and P 2p for NM95-H and NM95-L cathodes after activation between 2.7-4.3 V and 2.7-4.5 V.

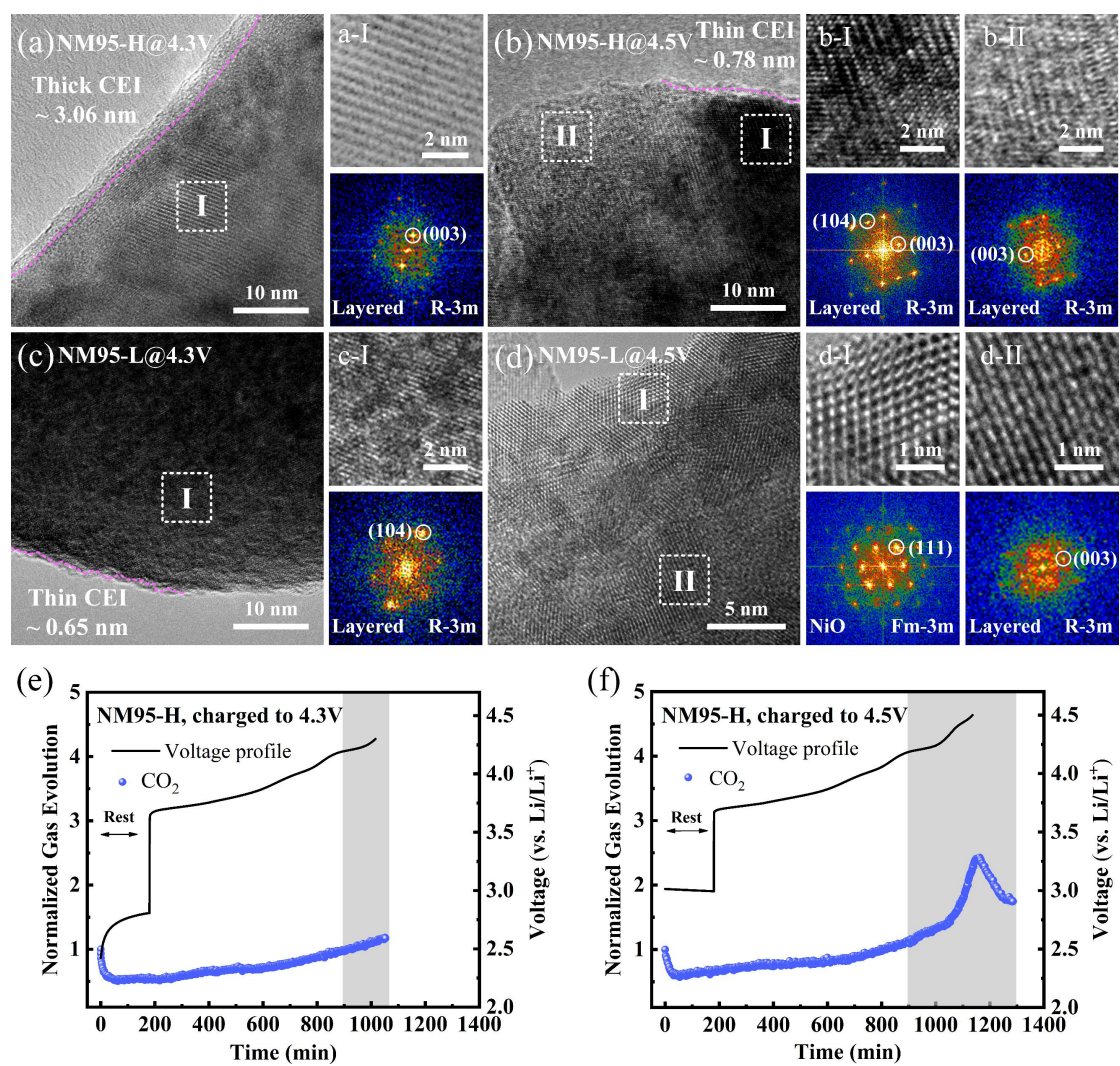


Fig. 4. TEM images of NM95-H after activation between (a) 2.7-4.3 V and (b) 2.7-4.5 V. TEM images of NM95-L after activation between (c) 2.7-4.3 V and (d) 2.7-4.5 V. Differential electrochemical mass spectrometry (DEMS) spectra of NM95-H cathode when charged to (e) 4.3 V and (f) 4.5 V at 0.1 C.

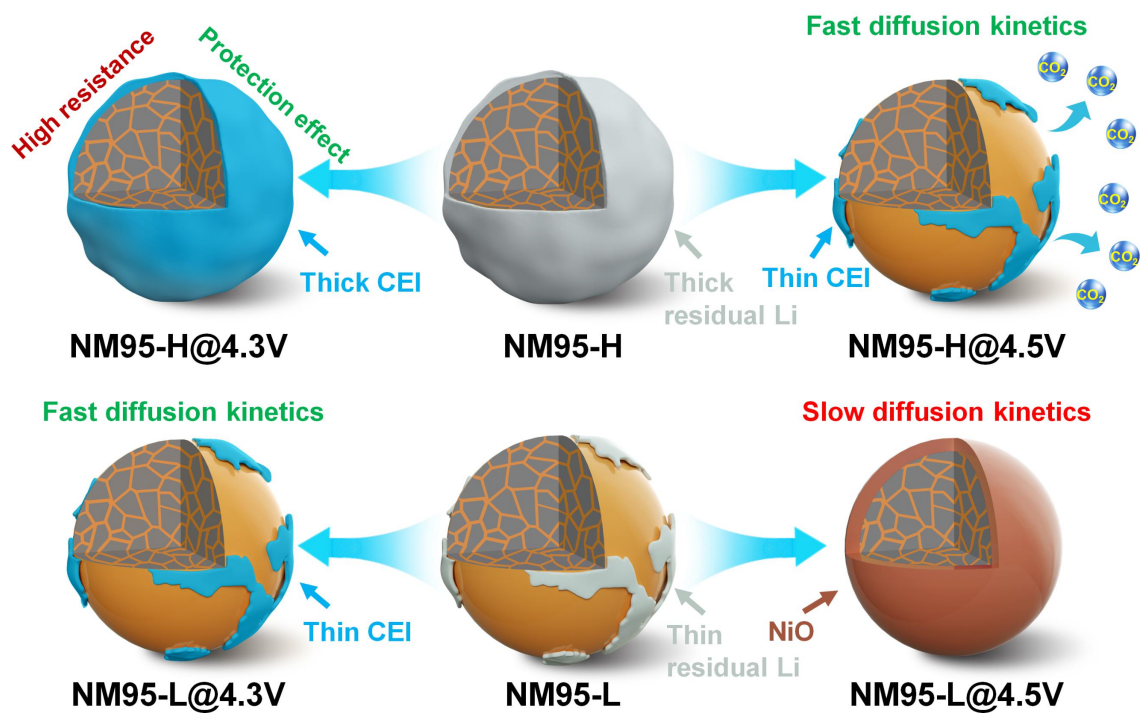


Fig. 5. Schematic illustrations of surface reconstruction of NM95-H and NM95-L cathodes after activation between 2.7-4.3 V and 2.7-4.5 V.

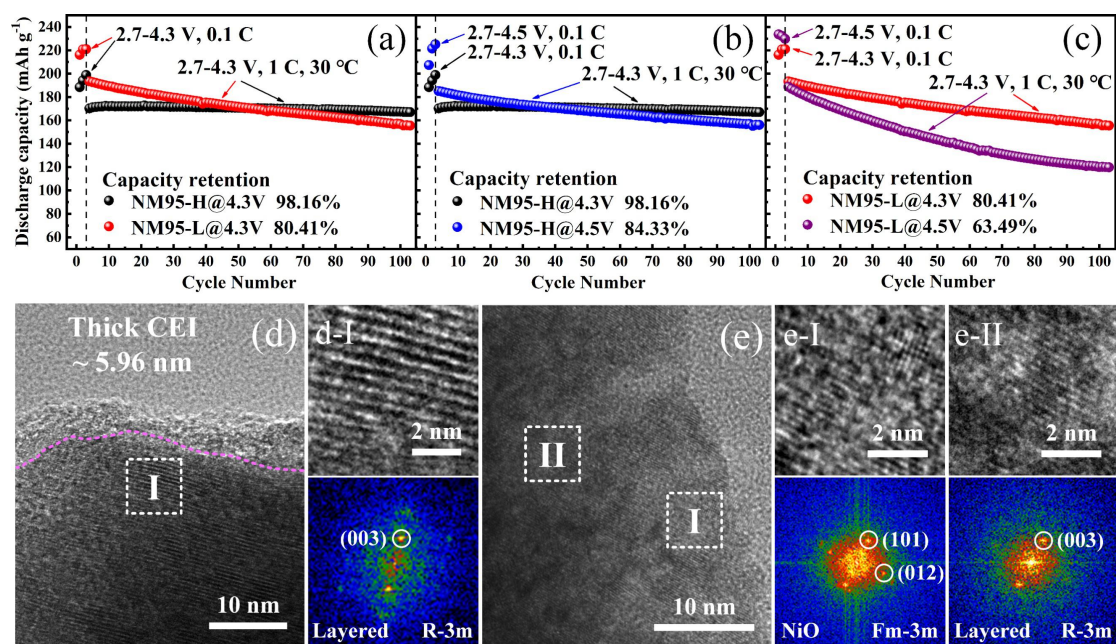


Fig. 6. (a) Cycling performance of NM95-H@4.3V and NM95-L@4.3V. Cycling performance of (b) NM95-H and (c) NM95-L activated at different voltage ranges. TEM image of (d) NM95-H@4.3V and (e) NM95-L@4.3V after 100 cycles between 2.7-4.3 V.

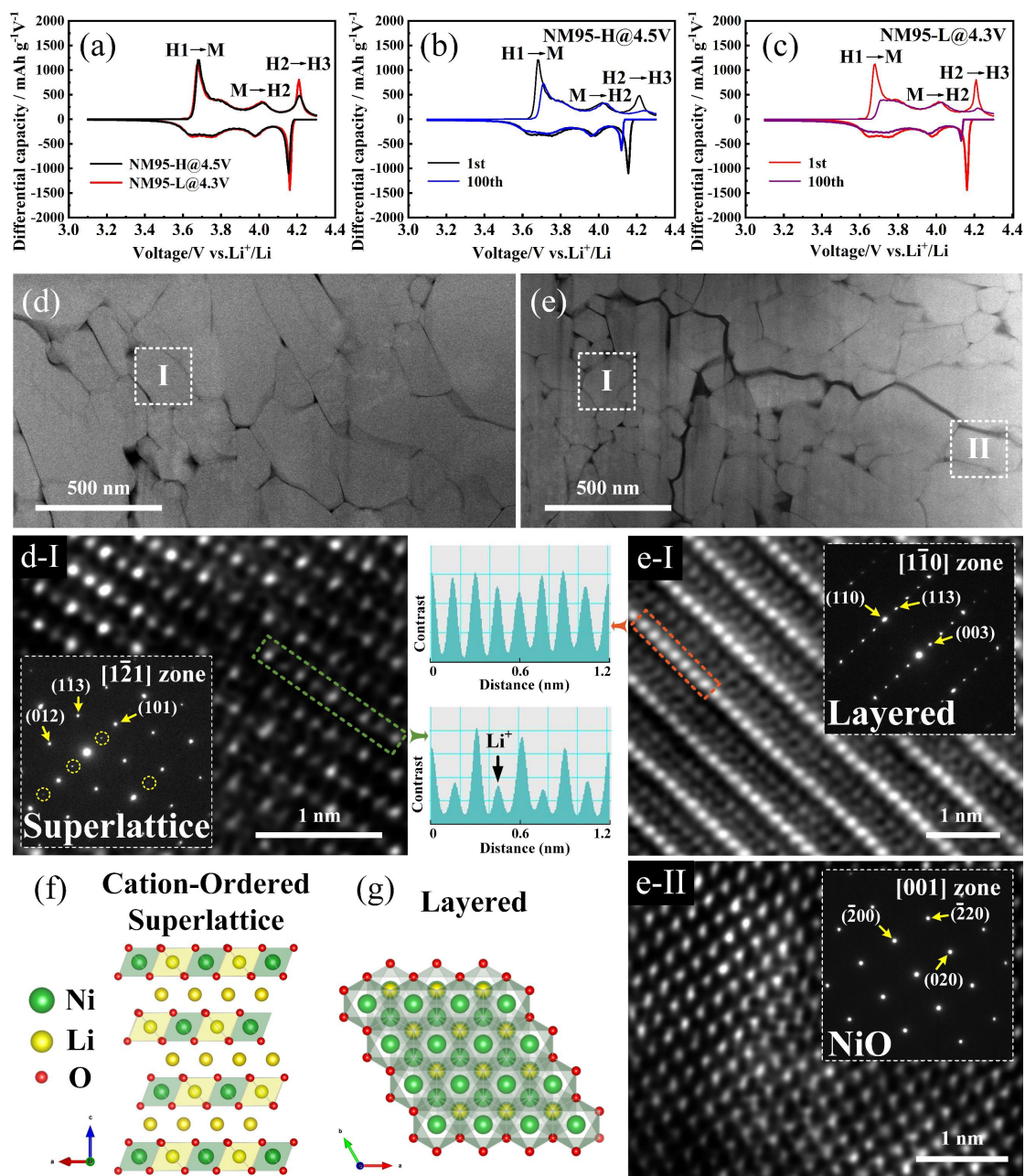
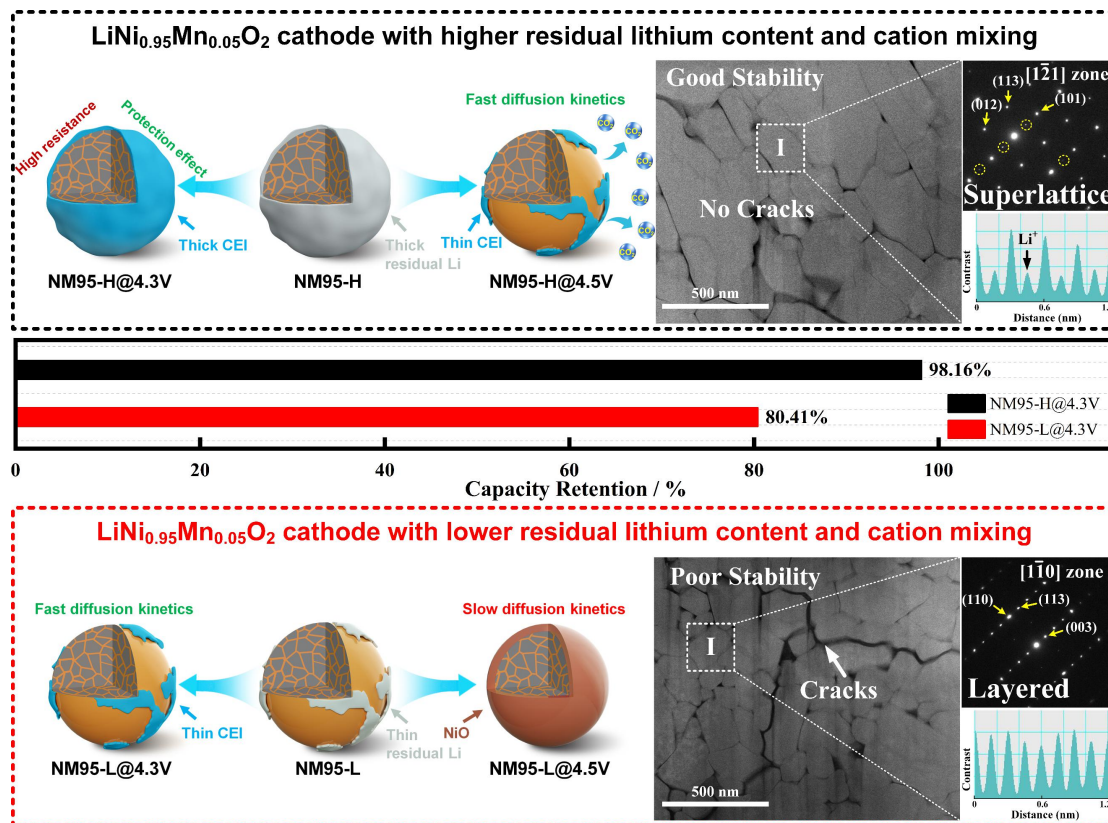


Fig. 7. (a) dQ/dV^{-1} curves of NM95-H@4.5V and NM95-L@4.3V during the first cycle between 2.7-4.3 V at 1 C. dQ/dV^{-1} curves of first and 100 cycles for (b) NM95-H@4.5V and (c) NM95-L@4.3V. Cross-section images of bulks of (d) NM95-H@4.5V and (e) NM95-L@4.3V cathodes at charged state after 100 cycles between 2.7-4.3V. STEM images of the marked area (d-I,e-I,e-II) with corresponding SAED patterns. Schematic illustrations of (f) cation-ordered and (g) layered structures corresponding to (d-I) and (e-I), respectively.

TOC

The residual Li can protect cathodes from electrolyte attack by converting to CEI below 4.3 V and the cation ordering structure impedes lattice collapse at a highly charged state.



Supporting Information

Unveiling the impact of residual Li conversion and cation ordering on electrochemical performance of Co-free Ni-rich cathodes

Chu Wang¹, Lei Tan², Hongling Yi¹, Zixiang Zhao¹, Xiaoli Yi³, Youyuan Zhou⁴,
Junchao Zheng³, Jiexi Wang³, Lingjun Li^{1,*}

¹ *School of Materials Science and Engineering, Changsha University of Science and Technology, Changsha, Hunan 410114, PR China*

² *School of Energy and Power Engineering, Changsha University of Science and Technology, Changsha, Hunan 410114, PR China*

³ *School of Metallurgy and Environment, Central South University, Changsha, Hunan 410083, PR China*

⁴ *Hunan Changyuan Lico Co. Ltd., Changsha, Hunan 410205, PR China*

* Corresponding author.

E-mail address: lingjun.li@csust.edu.cn (L. Li)

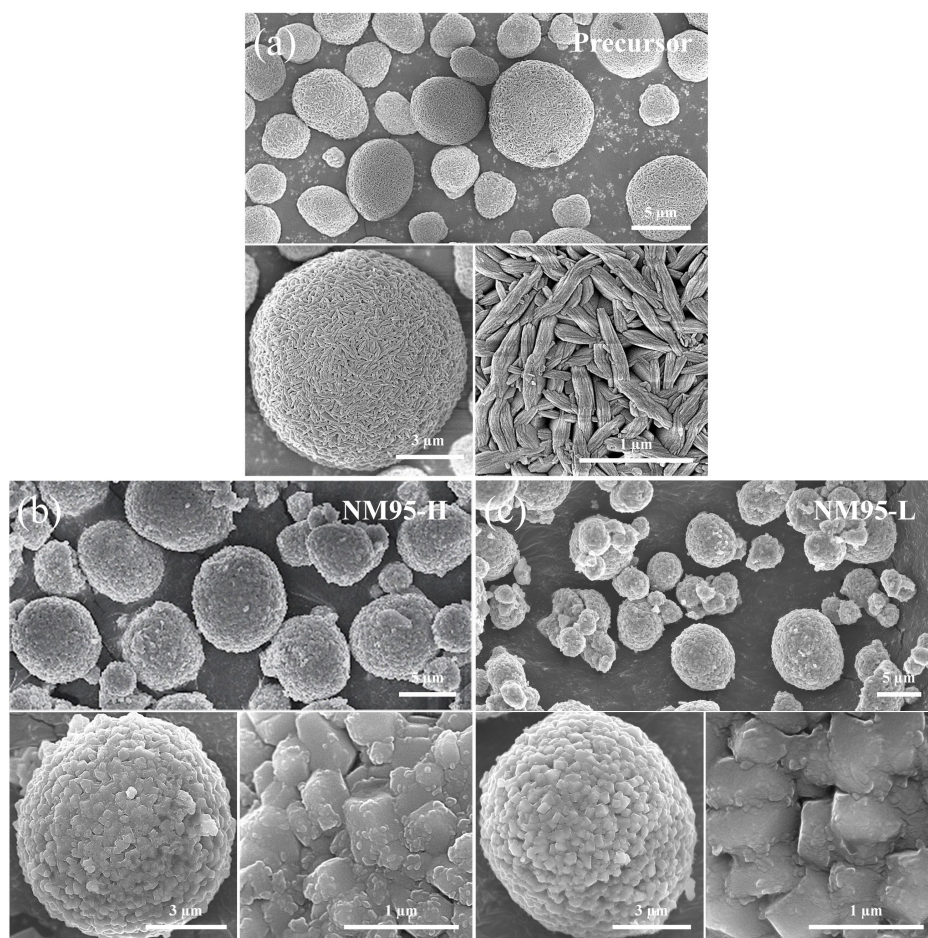


Fig. S1. SEM images of (a) precursor, (b) NM95-H and (c) NM95-L cathodes.

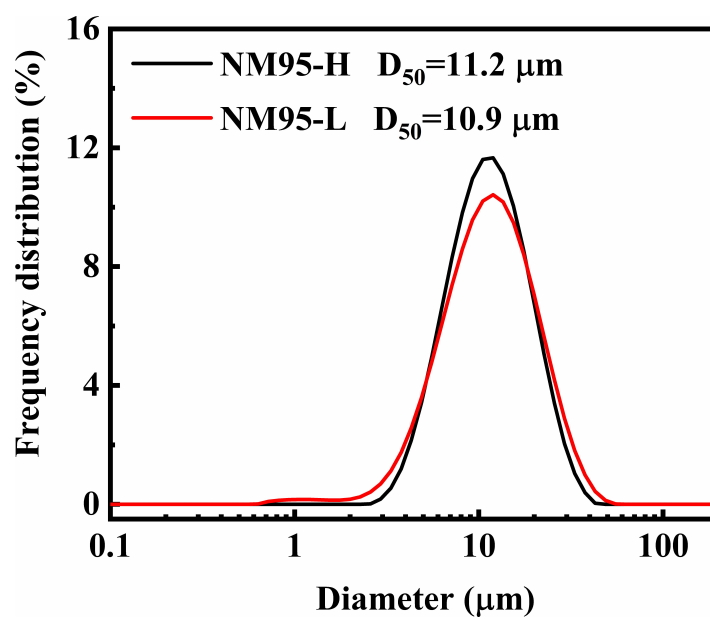


Fig. S2. Particle size distribution of NM95-H and NM95-L cathodes.

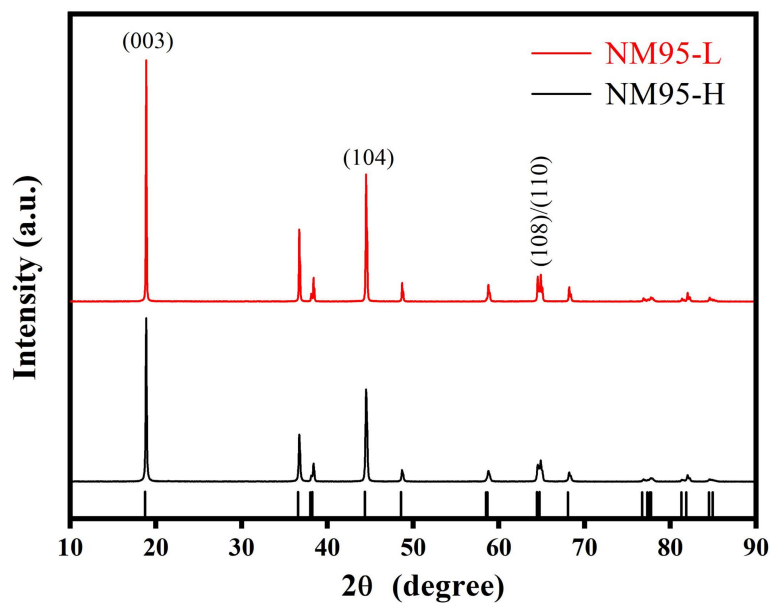


Fig. S3. XRD pattern of NM95-H and NM95-L cathodes.

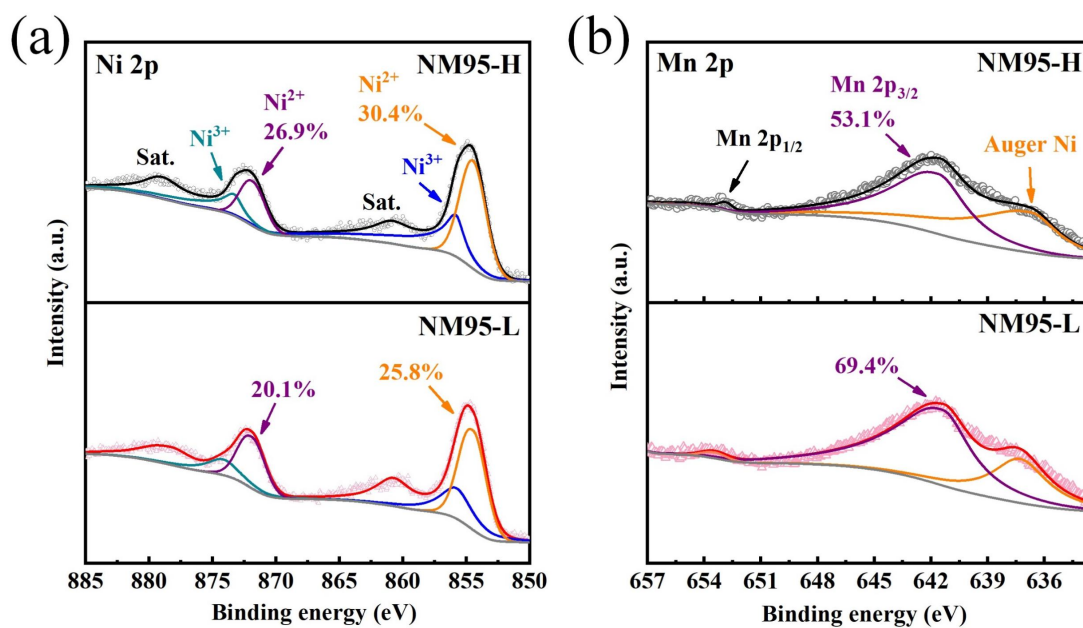


Fig. S4. XPS spectra of (a) Ni 2p and (b) Mn 2p for NM95-H and NM95-L cathodes.

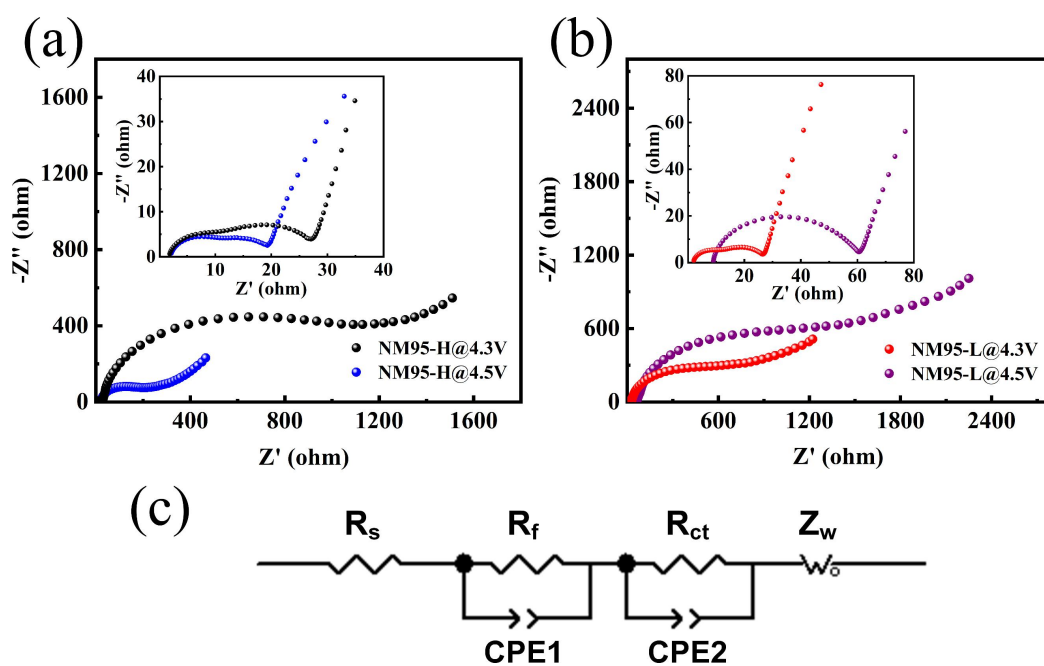


Fig. S5. EIS spectra of (a) NM95-H and (b) NM95-L cathodes after activations between 2.7-4.3 V and 2.7-4.5 V for 3 cycles. (c) Equivalent circuit.

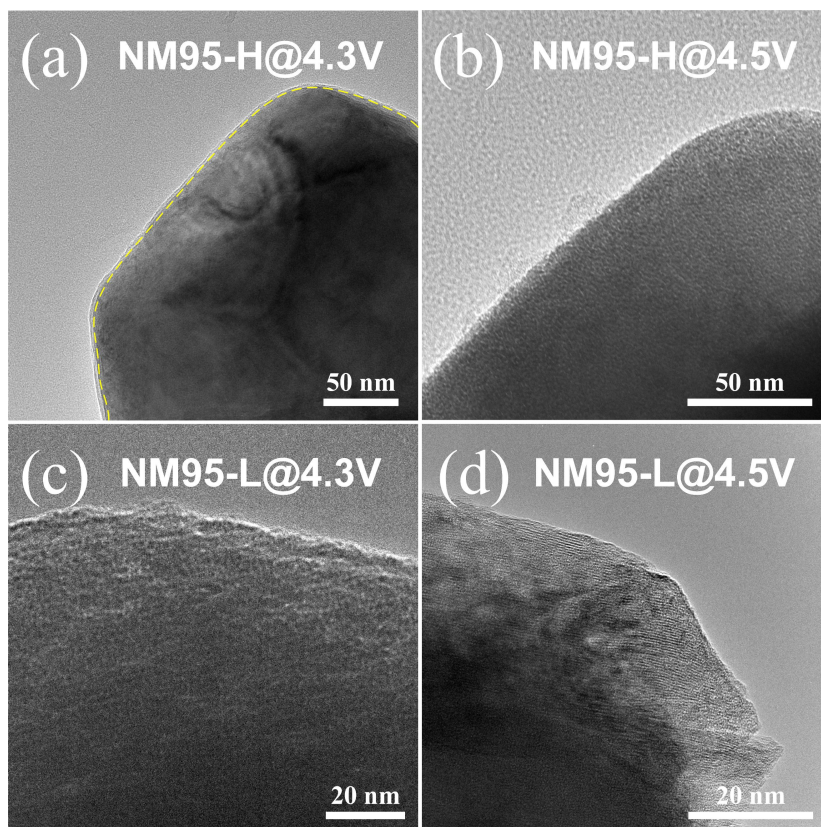


Fig. S6. (a-d) Low-magnification TEM images of CEI on electrochemically activated cathodes.

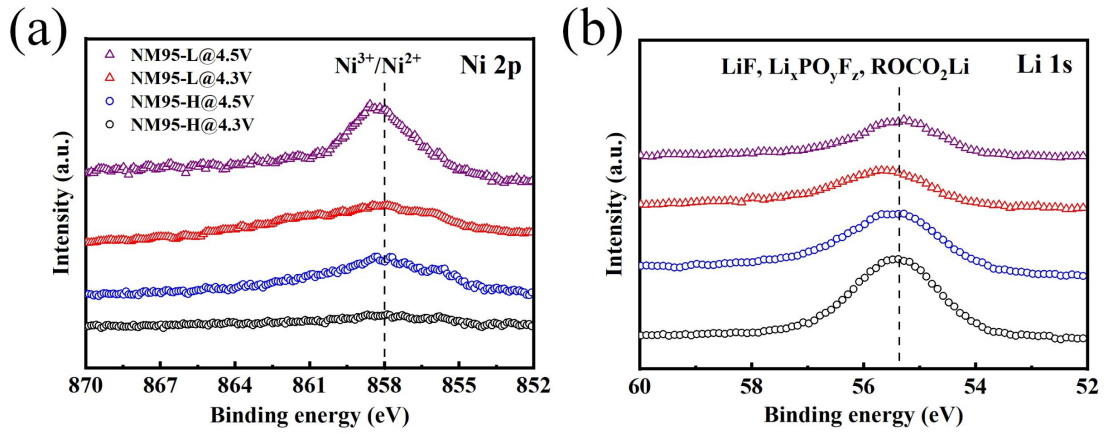


Fig. S7. XPS spectra of (a) Ni 2p and (b) Li 1s for NM95-H and NM95-L cathodes after activations between 2.7-4.3 V and 2.7-4.5 V for 3 cycles, respectively.

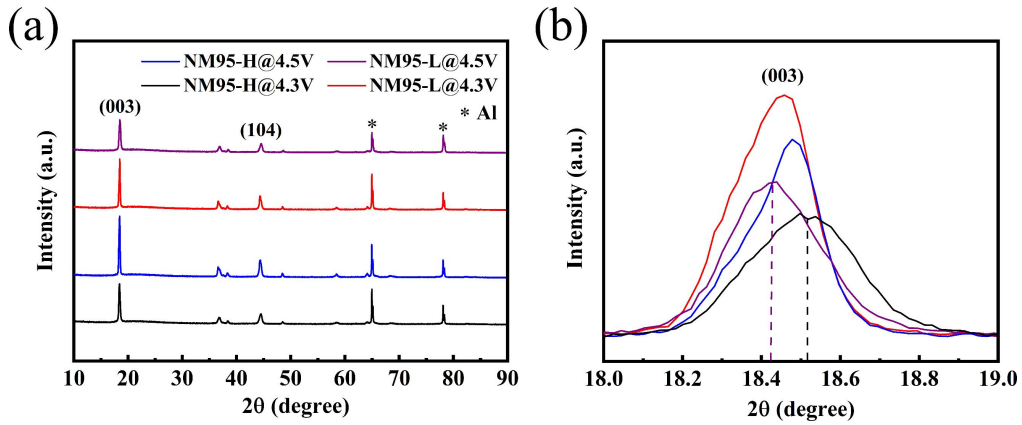


Fig. S8. (a) XRD patterns and (b) enlarged views of NM95-H and NM95-L cathodes after activations between 2.7-4.3 V and 2.7-4.5 V for 3 cycles.

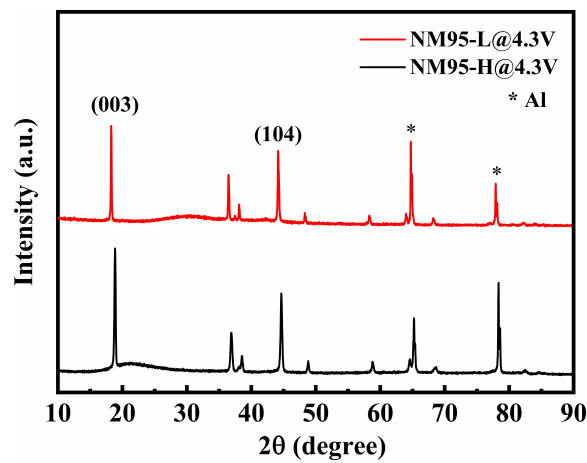


Fig. S9. XRD patterns of NM95-H@4.3V and NM95-L@4.3V cathodes after 100 cycles at 2.7-4.3 V.

Table S1 ICP-AES data of NM95-H and NM95-L cathodes

Sample	ICP-AES (molar ratio)		
	Li	Ni	Mn
NM95-H	1.0132	0.9512	0.0488
NM95-L	1.0125	0.9524	0.0476

Table S2 Rietveld refinement results of XRD data for NM95-H

NM95-H						
Volume: 101.2 Å ³		a-axis: 2.8765 Å			c-axis: 14.1964 Å	
Space group: R-3m		Rp = 4.191			Rwp = 5.649	
atom	site	X	Y	Z	B	Occ
Li1	3a	0	0	0.5	0.6	0.9554
Li2	3b	0	0	0	0.6	0.0445
Ni1	3a	0	0	0.5	0.6	0.0445
Ni2	3b	0	0	0	0.6	0.9054
Mn	3b	0	0	0	0.6	0.05
O	6c	0	0	0.2575	0.6	2

Table S3 Rietveld refinement results of XRD data for NM95-L

NM95-L						
Volume: 101.3 Å ³		a-axis: 2.8767 Å			c-axis: 14.1998 Å	
Space group: R-3m		Rp = 4.228			Rwp = 5.936	
atom	site	X	Y	Z	B	Occ
Li1	3a	0	0	0.5	0.6	0.9717
Li2	3b	0	0	0	0.6	0.0282
Ni1	3a	0	0	0.5	0.6	0.0282
Ni2	3b	0	0	0	0.6	0.9217
Mn	3b	0	0	0	0.6	0.05
O	6c	0	0	0.2575	0.6	2

Table S4 EIS fitting results of NM95-H and NM95-L cathodes

	R _f (Ω)	R _{ct} (Ω)
NM95-H@4.3	21.8	929.8
NM95-H@4.5	18.2	168.0
NM95-L@4.3	19.5	515.6
NM95-L@4.5	45.5	1053.0